



Highly Selective Production of Syngas from Chemical Looping Reforming of Methane with CO₂ Utilization on MgO-supported Calcium Ferrite Redox Materials

Vedant Shah^a, Zhuo Cheng^a, Deven S. Baser^a, Jonathan A. Fan^b, Liang-Shih Fan^{a,*}

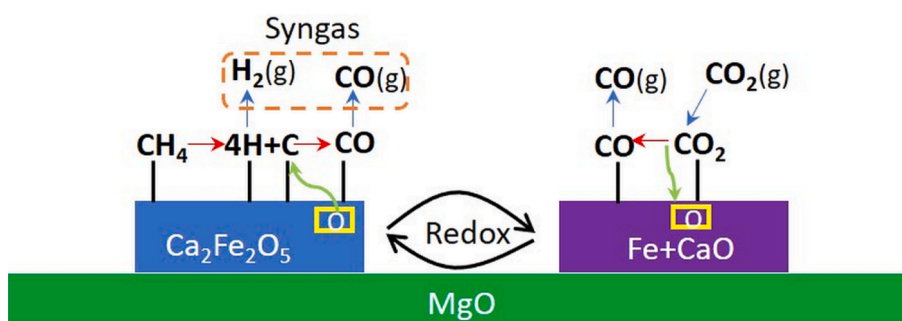
^a William G. Lowie Department of Chemical and Biomolecular Engineering, The Ohio State University, 151 West Woodruff Avenue, Columbus, OH 43210, USA

^b Department of Electrical Engineering, Ginzton Laboratory, Spiker Engineering and Applied Sciences, 348 Via Pueblo Mall, Stanford University, Stanford, CA 94305, USA

HIGHLIGHTS

- Use of MgO-supported calcium ferrite redox materials for simultaneous syngas production and CO₂ thermochemical splitting.
- >99% methane conversion with ~98% syngas selectivity and 2:1 H₂:CO ratio in a simulated co-current moving bed setup.
- CO₂ splitting to produce CO during reduced oxygen carrier regeneration close to thermodynamic limit of ~79%.
- The effect of oxygen vacancy concentration of Ca₂Fe₂O₅ on CH₄ activation and dissociation.
- The lattice oxygen in corner-sharing octahedra of Ca₂Fe₂O₅ acts as the efficient active sites for CO and H₂ production.

GRAPHICAL ABSTRACT



ARTICLE INFO

Keywords:

Chemical looping
Syngas production
CO₂ thermochemical splitting
Density functional theory

ABSTRACT

Chemical looping reforming with CO₂ splitting (CLRS) is an attractive process that can be used for conversion of hydrocarbons into syngas, an industrially important intermediate that serves as a building block for other value-added products. Under the chemical looping approach, the oxygen carrier that provides lattice oxygen, instead of molecular oxygen, is used for methane partial oxidation. This work focuses on MgO-supported Ca₂Fe₂O₅ redox materials as the oxygen carriers for simultaneous syngas production and CO₂ utilization through thermochemical CO₂ splitting using a two-reactor chemical looping system. We experimentally achieve a near 100% CH₄ conversion and a high syngas selectivity of >98%, which is by far the highest in chemical looping reforming systems. Complete regeneration of the reduced oxygen carriers is obtained using CO₂ with ~78% conversion, thereby operating close to the thermodynamic limit. Density functional theory calculations reveal that the lattice oxygen in corner-sharing octahedra of brownmillerite structure possessed by Ca₂Fe₂O₅ acts as the efficient active sites for CO and H₂ production. The formed oxygen vacancy significantly reduces the energy barriers of C-H cleavage and CO formation, leading to the reactivity and selectivity enhancement. MgO assists in reactivity enhancement by

* Corresponding author.

E-mail address: fan.1@osu.edu (L.-S. Fan).

<https://doi.org/10.1016/j.apenergy.2020.116111>

Received 15 July 2020; Received in revised form 27 September 2020; Accepted 23 October 2020

Available online 11 November 2020

0306-2619/© 2020 Elsevier Ltd. All rights reserved.

enabling higher degree of $\text{Ca}_2\text{Fe}_2\text{O}_5$ dispersion along with increasing $\text{Ca}_2\text{Fe}_2\text{O}_5$'s tolerance towards sintering. These findings will contribute to the systematic design of high-performance redox materials and chemical looping processes for syngas production with CO_2 utilization.

1. Introduction

Synthesis gas, or syngas is a mixture of hydrogen and carbon monoxide gas in varying proportions that acts as a feedstock for producing other value-added products like methanol, gasoline and higher hydrocarbons through Fischer-Tropsch synthesis, ammonia production, etc. [1]. Syngas is also used for producing hydrogen, which has gained importance in recent years because of its use as a clean fuel and a global push towards hydrogen-based economy [2]. Different technologies have been developed for the conversion of gaseous fuels like natural gas/shale gas into syngas and subsequent production of hydrogen. Some of these technologies are steam methane reforming (SMR), autothermal reforming (ATR), partial oxidation (POX), catalytic partial oxidation (CPOX) and dry methane reforming (DMR) [3]. Out of all the available technologies, SMR is predominantly used for syngas and hydrogen production [4]. The biggest drawback of SMR is burning of fossil fuels for generating the endothermic process heat well as the use of secondary shift reactors. CPOX makes use of a direct reaction between natural gas and molecular oxygen in the presence of a catalyst. As the reaction involved is exothermic, CPOX becomes more economically feasible. However, use of an air separation unit (ASU) to obtain molecular oxygen reduces the economic advantage of the process. Due to excessive exothermicity of the reaction, CPOX also involves risk associated with explosion. ATR is a good alternative for syngas and hydrogen production, which combines both SMR and CPOX processes to make an efficient, relatively low-temperature syngas producing technology [5]. The use of an air separation unit and the deactivation of the catalyst due to coking are some of the main challenges associated with this process [6]. Syngas produced from above-mentioned processes (primarily SMR) is fed into water-gas shift (WGS) membrane reactors, which help produce pure hydrogen with almost complete CO conversion and CO_2 capture [7]. Alternatively, energy intensive amine-based CO_2 removal is employed for commercial hydrogen production. A substantial amount of CO_2 generation leading to lower CO/ CO_2 ratio, the deviation from ideal H_2 :CO ratio of ~ 2.0 , and the use of processes such as sorbent-based CO_2 capture and WGS for upgrading syngas quality are major drawbacks with the syngas produced using conventional routes, rendering the syngas production and downstream processing highly capital intensive [8,9]. As CO is one of the major components of syngas with commercial importance, technologies have also been developed to harness it through thermochemical CO_2 splitting, where oxygen deficient metal oxides are regenerated in CO_2 to produce CO while minimizing the environmental impact [10]. CO produced in this manner can be used for carrying out processes of industrial importance such as carboxylation reactions. This method however has severe limitations like the use of extremely high temperatures and thermodynamic constraints for CO_2 utilization [11]. Incorporating CO_2 splitting to produce CO simultaneously along with high-purity syngas production can make the prospects of natural gas/shale gas conversion highly attractive.

Chemical looping reforming (CLR) is an alternative technology that has been developed for syngas and hydrogen production using carbonaceous fuels [12]. Gaseous fuels like natural gas, shale gas, reducing tail gases, etc. and solid fuels such as biomass, algae and coal have been used for syngas production through chemical looping [13–15]. Unlike ATR, POX, and CPOX that use molecular oxygen as an oxidant, CLR utilizes the lattice oxygen of the carriers as the oxygen source, thus eliminating the need to use an ASU. In conventional CLR process, the oxygen carrier is circulated between a fuel reactor and an air reactor. Methane is directly converted to syngas through oxygen carrier reduction and the reduced oxygen carriers are regenerated in air to complete a

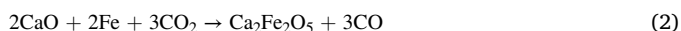
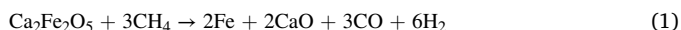
full cycle of the redox reaction. If the reduced oxygen carriers are oxidized using CO_2 instead of air, a CO-rich stream is obtained, where CO can be separated from CO_2 using pressure swing adsorption (PSA) or other equivalent technique [16]. This enables the chemical looping reforming of methane with CO_2 splitting (CLRS) for syngas production. The CO produced in this step can be used to adjust the H_2 :CO ratio of the syngas obtained from the reforming step based on the downstream production requirement or can be utilized independently for other processes as desired.

Oxygen carriers in the CLRS process are required to have high reactivity and recyclability, along with low cost and high mechanical strength with enough porosity for increased mobility of oxygen ions and reduced resistance to gas diffusion. Hundreds of materials have been screened in the past few decades [17] and transition metal oxides such as Fe_2O_3 have been identified as promising oxygen carriers for chemical looping reforming due to their high oxygen carrying capacity, good reactivity, and low cost [12]. However, the reactions of the transition metal oxides are complex as they involve occurrence of multiple oxidation states. As a result of the phase change, the crystal lattice undergoes volume contraction and expansion which leads to loss of activity and mechanical strength after multiple redox cycles [18,19]. Unmodified transition metal oxides like Fe_2O_3 oxygen carriers also lose reactivity due to sintering, which can be prevented by the addition of support material or dopants to the active metal oxide [20–22]. Addition of support is also known to prevent the segregation of phases and thus increase the stability of the oxygen carrier particles [23]. Support materials that are typically used along with iron-based oxygen carriers for the chemical looping reforming process include TiO_2 [24], Al_2O_3 , CeO_2 [25], SiO_2 [26], ZrO_2 [27], MgO , MgAl_2O_4 [20,28]. Perovskites are another class of oxygen carrier that have been employed for the chemical looping reforming process. The advantage of using perovskites is that they facilitate the quick movement of ions due to the availability of high vacancy concentration in the lattice [29], leading to an increased catalytic activity for methane conversion and enhanced selectivity towards syngas production. However, slow regeneration kinetics and loss of structural integrity over multiple redox cycles are major challenges associated with the use of perovskites as oxygen carriers in CLR scheme [30,31]. Mixed metal oxides have also been studied extensively for their use in the CLR process. Mixed metal oxides like Fe-Ni or Fe-Cu are known to have highly improved reduction kinetics due to the synergistic effect of both the active metal oxides. However, the major problem with these oxides is controlling selectivity towards syngas production [25,32]. Due to the thermodynamic constraints, this type of metal oxides requires the use of the three-reactor system for syngas production and CO_2 utilization as the oxides of metals like Fe, Cu or Ni cannot be regenerated fully in CO_2 [12,33].

Oxides of iron and calcium react with one another to form calcium ferrite ($\text{Ca}_2\text{Fe}_2\text{O}_5$) when added in stoichiometric amounts, a compound that is environmentally safe, chemically stable redox material and has been of particular interest in several chemical looping applications [34,35]. A study reported by Shah et al. showed increase in the process efficiency and exergy efficiency by $\sim 5.8\%$ (percentage points) using $\text{Ca}_2\text{Fe}_2\text{O}_5$ -assisted chemical looping reforming of natural gas as compared to syngas production using autothermal reforming [36,37]. Liu et al. investigated the use of calcium ferrites with microalgae as the carbon source for syngas production and obtained syngas with high selectivity through steam co-injection [38]. The effects of dopants like Cu, Ni, Sr, and Co on calcium ferrite for algae gasification and hydrogen production have been studied by Liu et al. and Hosseini et al. [39,40]. The study showed that the addition of dopants led to an enhancement in

the reactivity of $\text{Ca}_2\text{Fe}_2\text{O}_5$, thus increasing the syngas and hydrogen yields. The use of $\text{Ca}_2\text{Fe}_2\text{O}_5$ for producing hydrogen and syngas using CO [41] and pine wood [42], respectively with biomass utilization has been investigated by Sun et al. [43]. Their results showed an increase in the H_2 yield and carbon conversion with a substantial improvement in the total gas yield. Table 1 shows a quantitative comparison between the syngas generation performance of different oxygen carriers through chemical looping gasification/reforming. It must be noted that for some of the reported cases, steam and/or CO_2 has been co-fed along with the hydrocarbon feedstock to enhance syngas yield. None of the oxygen carriers reported in Table 1 simultaneously achieve full feedstock conversion along with optimum quality syngas generation such that it can be directly utilized for the downstream F-T process. Although $\text{Ca}_2\text{Fe}_2\text{O}_5$ has been previously investigated for syngas generation using chemical looping, dominant research has been focused on the utilization of biomass and related feedstocks. To our knowledge, no optimized system has been reported in the literature for partially oxidizing CH_4 to produce high-purity syngas along with CO_2 utilization using $\text{Ca}_2\text{Fe}_2\text{O}_5$. In addition, the mechanism underlying their activity remains unclear.

This work comprehensively investigates the activity of $\text{Ca}_2\text{Fe}_2\text{O}_5$ for CH_4 conversion and CO_2 splitting using the novel CLRS system as shown in Fig. 1. Two reactions expected to occur for simultaneous production of syngas and thermochemical CO_2 splitting are:



The effect of multiple redox cycles on the reactivity and morphology of the oxygen carriers was studied using thermogravimetric analyzer (TGA) and characterization techniques like X-ray diffraction (XRD), scanning electron microscope (SEM) and energy dispersive X-ray spectroscopy (EDS). Experiments were conducted in a co-current simulated moving bed setup with outlet gas concentrations being measured to assess methane conversion, syngas yield, and H_2/CO ratio. Atomistic thermodynamics combined density functional theory calculation also was performed to explore the mechanism for calcium ferrite reactivity enhancement. The results provide a better understanding of the underlying solid-state chemistry which is essential for the design and development of robust oxygen carriers that exhibit high reactivity and selectivity.

2. Experimental section

2.1. Sample preparation

$\text{Ca}_2\text{Fe}_2\text{O}_5$ was prepared by mixing the oxides of calcium and iron in

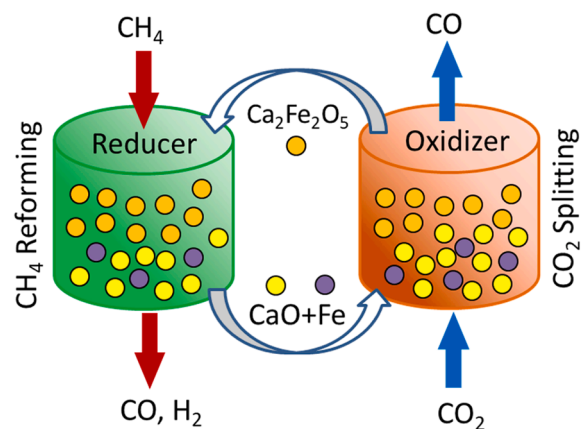


Fig. 1. Schematic representation for chemical looping reforming with CO_2 splitting (CLRS) process.

the ratio 2:1 by mole and using the solid-state synthesis technique. Desired weight of iron and calcium oxide powders (Noah Technologies, 99.9% pure, and 3–5 μm in size) was measured and the powders were mixed together thoroughly in a ball mill so that they could be mechanically activated to obtain high surface energy and reduced grain size. Deionized water was added to the powder mixture to convert it into paste, which was dried at 150 $^\circ\text{C}$ in an oven for 60 min. The solids obtained were crushed and sintered at various temperatures for varying times to obtain high purity $\text{Ca}_2\text{Fe}_2\text{O}_5$ phase. Based on results from different samples, it was found that sintering the powders at 1150 $^\circ\text{C}$ for 10 h gave the best results with an extremely high phase purity, as observed using XRD. The MgO-supported oxygen carriers were prepared using a similar method by varying the MgO concentration. Various oxygen carrier samples synthesized along with their oxygen carrying capacity (OCC) are reported in Table 2. OCC is defined as the number of

Table 2
Oxygen carrier samples with different compositions.

Sample Name	Composition (wt. %)		Phase purity (%)		OCC (mol/mol basis)
	$\text{Ca}_2\text{Fe}_2\text{O}_5$	MgO	At eq.	From TGA	
CF-0 Mg	100	0	100	97.07	3
CF-10 Mg	90	10	100	~98.0	3
CF-20 Mg	80	20	100	~98.0	3
CF-40 Mg	60	40	100	~98.4	3

Table 1
Syngas generation comparison amongst different oxygen carriers.

Oxygen carrier	Reactor configuration	Feedstock	Fuel conversion (%)	Syngas purity (%)	H_2/CO	Ref.
Ni/ CeO_2	Fixed-bed reactor	CH_4	~80	90.9	2.2	[44]
Iron ore	Fluidized bed reactor	Biomass	–	~70	~2.45	[45]
Ni-doped $\text{Fe}_2\text{O}_3/\text{Al}_2\text{O}_3$	Fixed-bed reactor	$\text{CH}_4 + \text{CO}_2$	95	~96	~2.3	[46]
$\text{BaCoO}_{3.8}/\text{CeO}_2$	Fixed-bed reactor	CH_4	–	94.5*	~2	[47]
$\text{Mn}/\text{ZrO}_2/\text{Al}_2\text{O}_3$	Fixed-bed reactor	$\text{CH}_4 + \text{CO}_2$	~99	~70*	~2.5	[48]
$\text{NiO}/\text{Al}_2\text{O}_3$	Internally circulating reactor	CH_4	91.7	84.1	2.16	[49]
$\text{Fe}_2\text{O}_3/\text{Al}_2\text{O}_3$	Tube reactor	Rice straw	85	~76	~2.25	[50]
$\text{CuO}/\text{Fe}_2\text{O}_3/\text{Al}_2\text{O}_3$	Fixed-bed reactor	CH_4	76.3	84	1.6	[33]
$\text{LaNi}_{1-x}\text{Fe}_x\text{O}_3$	Tube reactor	acetic acid	~70	~74	~6	[51]
Fe_2O_3 -phosphogypsum	Fixed-bed reactor	Lignite	~98	–	~0.6	[52]
$\text{Ca}_2\text{Fe}_2\text{O}_5$	Fixed-bed reactor	Microalgae + steam	–	~70	~6	[38]
$\text{Ca}_2\text{Fe}_2\text{O}_5$	Fixed-bed reactor	Pine wood	~90	–	~9	[42]
$\text{Ca}_2\text{Fe}_2\text{O}_5/\text{Zn}$	Fixed-bed reactor	Biomass + steam	–	~77	~2.4	[53]
$\text{Ca}_2\text{Fe}_2\text{O}_5$	Fixed-bed reactor	Biomass + steam	–	~74	~6	[54]
$\text{CaO}/\text{Fe}_2\text{O}_3/\text{Al}_2\text{O}_3$	Fluidized bed reactor	Coal Tar	~85	~82	~1.3	[55]
$\text{Ca}_2\text{Fe}_2\text{O}_5/\text{MgO}$	Co-current moving bed reactor	CH_4	99.88	98.08	2.03	This work

* CO selectivity.

H_2 yield.

moles of lattice oxygen available per mole of $\text{Ca}_2\text{Fe}_2\text{O}_5$ in the sample. Labelling of the oxygen carriers has been done as CF-xMg, where 'x' shows the wt% of MgO present in the oxygen carrier. MgO was selected as it did not react with either calcium or iron and is known to be a thermally stable metal oxide at high temperatures as seen from the phase diagram plotted in Fig. S1. CaO-based oxygen carriers tend to lose their reactivity across multiple redox cycles due to sintering occurring at high temperature, which is a well-known problem reported in the literature [56,57]. Consequently, a support material (MgO) has been added to the $\text{Ca}_2\text{Fe}_2\text{O}_5$ -based oxygen carrier samples to investigate its effect on the reactivity and the sintering resistance as inert metal oxide supports are known to provide high-surface area to active metal oxide, thus enhancing reaction rates. Moreover, MgO also helped to increase the heat carrying capacity of the oxygen carrier, a parameter critical for ensuring adiabatic operation of the chemical looping system [58,59].

2.2. TGA experiments

The reactivity of different oxygen carrier samples was tested using Setaram SETSYS Evolution TGA by allowing the samples to undergo 10 continuous reduction-oxidation (redox) cycles. All the experiments conducted in the TGA were performed at 1000 °C. The rationale of choosing this temperature for carrying out the experiments is based on the thermodynamic constraints as explained in Section 3. The temperature was ramped up from room temperature to 1000 °C at 55 °C/min under N_2 flow of 100 ml/min. He flowrate was set to 50 ml/min during reduction and oxidation, which is used as protective gas for the TGA to make sure no reducing gases entered the sensitive weighing balance of the TGA placed at its top. Once the target temperature was reached, CH_4 was injected into the TGA with total flowrate of 187.5 ml/min comprising of 20% CH_4 , rest balanced with N_2 and He. Regeneration of the reduced oxygen carrier samples was done by sending gas with total flowrate of 250 ml/min into the reactor with 40% CO_2 , rest balanced with N_2 and He. Reduction time was set to 2 min and oxidation was carried out for 10 min to ensure complete regeneration of reduced samples. N_2 was flown at 100 ml/min between reduction and oxidation steps for 2.5 min to flush out the reactor. Total sample weight for different oxygen carriers was kept between 30 and 35 µg. Small sample size of solids and high gas flowrates were used to eliminate any mass transfer limitations during the experiments. The oxygen carrier samples were subjected to H_2 -TPR (Temperature programmed reduction) to investigate the improvement in their reactivity due to MgO incorporation. CH_4 was not used as the reducing agent for TPR as temperature <720 °C would have led to formation of CaCO_3 , which would have decomposed at higher temperatures, thus making it difficult to understand the oxidizing capability of the oxygen carrier though weight change data analysis. H_2 -TPR was carried out by mounting 30–35 µg sample on crucible and sending 250 ml/min gas mixture containing 5% H_2 through the TGA, rest balanced with He and N_2 . The temperature was initially ramped from room temperature to 400 °C at 30 °C/min and maintained isothermally with N_2 -only flow for 30 min to ensure desorption of any moisture or air. Temperature was then ramped from 400 °C to 1000 °C at 5 °C/min while injecting H_2 - N_2 mixture. TGA chamber was flushed with N_2 before starting the experiment to ensure air was completely removed.

2.3. Simulated co-current moving bed experiments

Experiments were carried out in a fixed bed setup to analyse outlet gas compositions and critical parameters such as methane conversion, dry syngas selectivity and H_2 :CO ratio. A simulated co-current moving bed type of arrangement was made to mimic the performance of an actual chemical looping reducer. Once reduced, the solids were oxidized back in CO_2 for regeneration. Although oxidation was carried out in a fixed bed mode, a fluidized bed must be employed in a commercial setup to ensure complete oxidation of the reduced particles as well as their

pneumatic transport. Freshly prepared oxygen carrier samples were first reduced in hydrogen to obtain reduced samples. The top of the bed was loaded with fully oxidized oxygen carrier samples whereas the bottom of the bed was filled with H_2 -reduced samples, while both the layers were separated using quartz wool. This configuration was chosen to mimic the solids profile as seen in the moving bed reactor. The reduced and oxidized particles were used in the ratio 1:3 with total sample loading of 2 g, such that the gas hourly space velocity (GHSV) remained constant at 1500 h^{-1} . CH_4 -Ar mixture with a total flowrate of 25 ml/min was sent into the ceramic reactor with 10% methane concentration. Outlet gases containing CH_4 , H_2 , CO and CO_2 were measured using QMS, MKS Cirrus 2 mass spectrometer (MS). Tube furnace was used to heat the reactor with ramp rate of about 25 °C/min up to 1000 °C (operating temperature), upon which CH_4 -Ar mixture was injected into the system. Reaction was allowed to proceed until $\text{H}_2/(\text{CO} + \text{CO}_2) < 2$ condition was maintained and the amount of CO_2 coming out of the reactor was minimum (<1%). To carry out regeneration of the reduced oxygen carriers, 25 ml/min CO_2 -Ar mixture with 40% CO_2 was used. CO and CO_2 gas concentrations were measured using the MS to evaluate CO_2 uptake and calculate conversion.

2.4. Oxygen carrier sample characterization

XRD, SEM and EDS characterization techniques were used to analyze fresh as well as post-reaction oxygen carrier samples to see the effect of the reaction conditions on the oxygen carrier morphology. SEM/EDS was carried out using the FEI Quanta 200 scanning electron microscope. Accelerating voltage of 25.0/30.0 kV and spot size of 4.0/5.0 was set for obtaining the images. Similarly, voltage and spot size of 25.0 kV and 6.0 was used for EDS analysis. Rigaku SmartLab diffractometer was used for performing XRD on the solid samples. All the samples were scanned from 10 to 75° at 1 degree per minute. Accelerating voltage of 40 kV and filament current of 44 mA was used during all the scans. The XRD spectra was generated by attaching a diffracted beam monochromator (DBM) to the detector bracket to reduce the sample fluorescence.

2.5. Density functional theory (DFT) calculations

The first-principle calculations were performed within the framework of density functional theory (DFT), using the Vienna Ab Initio Simulation Package (VASP) [60–62]. The generalized gradient approximation of Perdew, Burke and Ernzerhof (PBE) was used to represent the exchange–correlation energy [63]. The projector-augmented wave (PAW) method, with a 400 eV energy cut-off was used to describe the wave functions of the atomic cores [64,65]. The valence electron configurations that were used are $3s^2 3p^6 4s^2$ for Ca, $3d^7 4s^1$ for Fe, and $2s^2 2p^4$ for O. The tetrahedron method with Blöchl corrections was used to set the partial occupancies for the orbitals [66]. A $5 \times 5 \times 5$ Monkhorst-Pack mesh was used during the structural relaxations. The on-site Coulomb repulsion amongst the localized 3d electrons is not described very well in a spin-polarized DFT treatment. To consider this Coulomb repulsion explicitly, a Hubbard U correction of 4 eV was applied [67,68]. The oxygen vacancy formation energies were calculated based on the following equation:

$$E_f = E_{\text{tot}} - E_V - \frac{1}{2}E_{\text{O}_2} \quad (3)$$

In Eq. (3), E_{tot} is the total energy of the stoichiometric surface, E_V is the total energy of the reduced surface with one oxygen vacancy, and E_{O_2} is the total energy of the optimized gas phase O_2 . The adsorption energy of adsorbate (E_{ad}) is defined as the total energy difference between before and after the molecular adsorption at each surface.

$$E_{\text{ad}} = E_A + E_{\text{surf}} - E_{(\text{A}+\text{surf})} \quad (4)$$

where E_{surf} is the total energy of the clean slab, E_A is the total energy of an

isolated adsorbate in the gas phase, and $E_{(A+surf)}$ is the total energy of the slab with adsorbed species. The climbing-image nudged elastic band (CI-NEB) method was used to locate transition states and map out reaction pathways for CH_4 partial oxidation on $\text{Ca}_2\text{Fe}_2\text{O}_5$ [69,70]. This method enabled the stationary points to be mapped out along the minimum energy paths and identified transition states for each of the diffusion processes.

3. Results and discussion

3.1. Thermodynamic analysis of CLRS

The thermodynamic analyses of the various reactions involved in this process was done using the thermochemical software Factsage v7.3 [71]. Change in the Gibbs free energy was plotted as a function of temperature for both the complete and partial oxidation of methane using $\text{Ca}_2\text{Fe}_2\text{O}_5$ to investigate the thermodynamic feasibility of the reactions as shown in Fig. 2a. The change in Gibbs free energy for partial oxidation is much more negative as compared to that of complete oxidation reaction, suggesting partial oxidation of methane using $\text{Ca}_2\text{Fe}_2\text{O}_5$ to form syngas is thermodynamically favoured. At temperatures greater than 683°C , methane reacts with the oxygen carrier to form limited amount of CO_2 . The change in Gibbs free energy for partial oxidation of methane using Fe_2O_3 (-136.8 kJ/mol at 1000°C) was less negative as compared to $\text{Ca}_2\text{Fe}_2\text{O}_5$ (-280.1 kJ/mol at 1000°C) as shown in Fig. 2b, implying the thermodynamic superiority of the CaO-modified Fe_2O_3 based oxygen carrier ($\text{Ca}_2\text{Fe}_2\text{O}_5$). Similar plot was made to assess the thermodynamic feasibility of the reactions between $\text{Ca}_2\text{Fe}_2\text{O}_5$ and H_2 and CO , as shown in Fig. S2 of the supplementary section. The change in Gibbs free energy is positive, suggesting that the reaction between H_2/CO and $\text{Ca}_2\text{Fe}_2\text{O}_5$ is thermodynamically unfavorable. This is highly desirable as CH_4 would react with $\text{Ca}_2\text{Fe}_2\text{O}_5$ to produce H_2 and CO , which will not react readily with $\text{Ca}_2\text{Fe}_2\text{O}_5$, leading to a high selectivity

towards syngas formation. Factsage was also used to assess the equilibrium composition data at 1 atm with varying temperatures where 1 mol of $\text{Ca}_2\text{Fe}_2\text{O}_5$ and 3 mol of CH_4 was used as input for the simulation and the number of moles of product species obtained were plotted as a function of temperature. Following equations were used to evaluate the useful parameters of the reducer:

$$\text{Methane conversion (\%)} = \frac{\text{CH}_{4,\text{in}} - \text{CH}_{4,\text{out}}}{\text{CH}_{4,\text{in}}} \times 100 \quad (5)$$

$$\text{Syngas selectivity (dry basis) (\%)} = \frac{\text{H}_{2,\text{out}} + \text{CO}_{,\text{out}}}{\text{H}_{2,\text{out}} + \text{CO}_{,\text{out}} + \text{CO}_{2,\text{out}} + \text{CH}_{4,\text{out}}} \times 10 \quad (6)$$

$$\text{H}_2 : \text{CO ratio} = \frac{\text{H}_{2,\text{out}}}{\text{CO}_{,\text{out}}} \quad (7)$$

$$\text{Carbon deposition (\%)} = \frac{\text{C}_{,\text{out}}}{\text{CH}_{4,\text{in}}} \times 100 \quad (8)$$

$$\text{CO}_2 \text{ conversion (\%)} = \frac{\text{CO}_{2,\text{in}} - \text{CO}_{2,\text{out}}}{\text{CO}_{2,\text{in}}} \times 100 \quad (9)$$

n_{out} and n_{in} refers to number of moles of species 'n' exiting and entering the reactor, respectively. Fig. S3 shows the increase in methane conversion and syngas selectivity with an increase in the temperature, which can be attributed to the endothermic nature of the reaction. Operating temperatures $>900^\circ\text{C}$ in the reducer helped to achieve $>97.5\%$ methane conversion with syngas selectivity as high as 99.5% with $\sim 2:1$ $\text{H}_2:\text{CO}$ ratio. Thus, operating temperature of 1000°C was used for all the experiments performed. To understand the effect of oxygen carrier to fuel ratio at 1000°C under atmospheric pressure, thermodynamic simulation was set up in Factsage where CH_4 input was

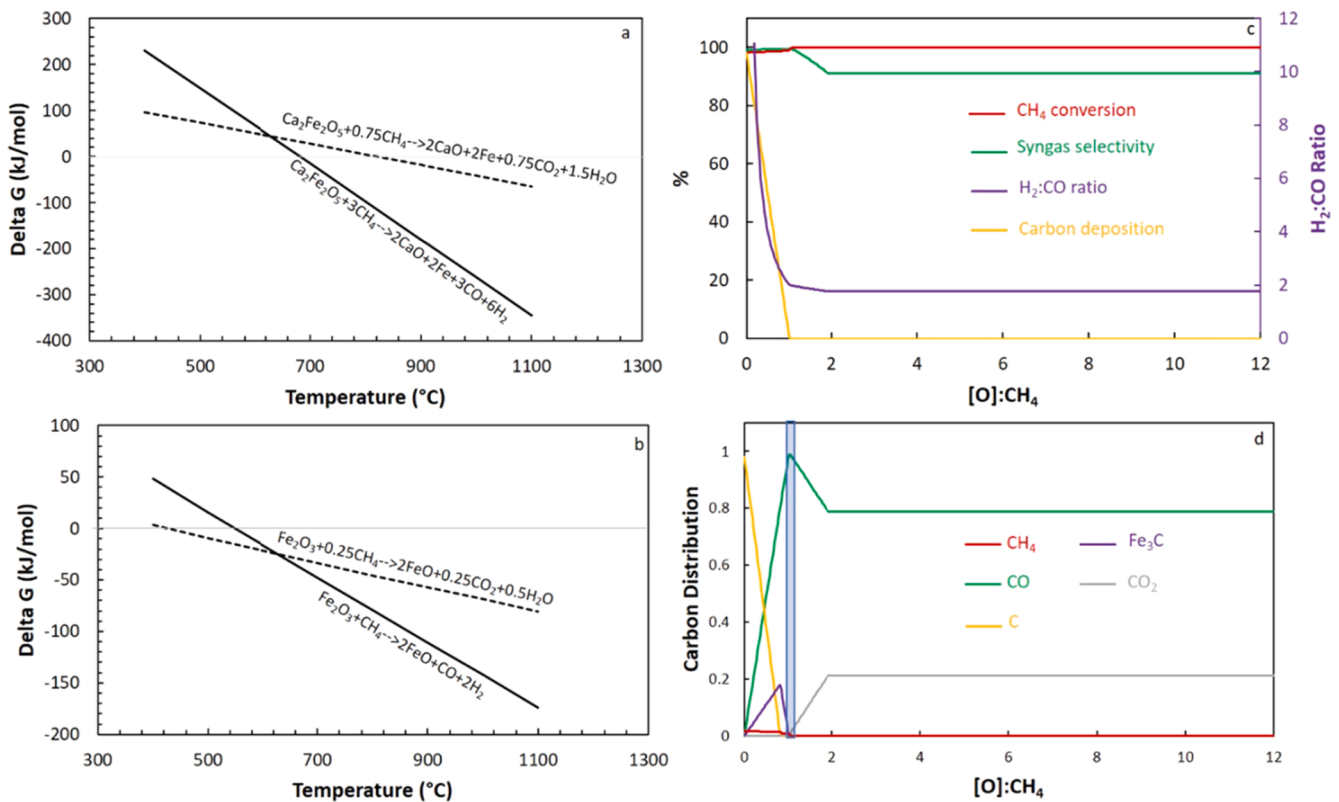


Fig. 2. Gibbs free energy vs. Temperature for (a) $\text{Ca}_2\text{Fe}_2\text{O}_5$ and (b) Fe_2O_3 with effect of $[\text{O}]:\text{CH}_4$ mass ratio on (c) conversion, selectivity and $\text{H}_2:\text{CO}$ ratio and (d) equilibrium carbon distribution.

fixed at 1 mol and number of moles of $\text{Ca}_2\text{Fe}_2\text{O}_5$ were varied from 0 to 4. Fig. 2c shows change in methane conversion, syngas selectivity, $\text{H}_2:\text{CO}$ ratio and carbon deposition with change in $[\text{O}]:\text{CH}_4$ ratio, where $[\text{O}]$ refers to the lattice oxygen available with $\text{Ca}_2\text{Fe}_2\text{O}_5$ that can take part in the reaction. Methane conversion $>99\%$ and 99% selectivity towards syngas with $\text{H}_2:\text{CO}$ ratio of $\sim 2:1$ is obtained at $[\text{O}]:\text{CH}_4$ ratio of 0.98. When $[\text{O}]:\text{CH}_4$ ratio >0.98 is used, the carbon deposition can be minimized but selectivity towards syngas drops as the amount of CO_2 increases, as evident from the carbon distribution shown in Fig. 2d. As the amount of $[\text{O}]$ increases, the formation of CO_2 becomes thermodynamically favorable due to the availability of oxygen from the oxygen carrier. Shaded region in Fig. 2d represents the region suitable for syngas production. This information aids in estimating the ratio of solid (oxygen carrier particles) circulation rate to methane feed for an actual operation in a co-current moving bed integrated chemical looping system such that the product gases at reducer outlet are in equilibrium only with the desired solid phases of the oxygen carrier particles. Two plateaus seen in the 'syngas selectivity' curve from Fig. 2c show the presence of different oxidation states of Fe. Fe mostly exists as Fe_3C with extremely tiny fraction of Fe (0) in the region represented by plateau on the left. Oxidation state changes to Fe (0) in the transition region between the two plateaus. Fe is present as both Fe (III) and Fe (0) under the region corresponding to second plateau on right. This is because the $\text{Ca}_2\text{Fe}_2\text{O}_5\text{-CH}_4$ mixture is fuel-lean, making it impossible for methane to reduce the oxygen carrier completely.

Apart from the high-quality syngas generation using methane, enhanced CO_2 utilization is another advantage offered by $\text{Ca}_2\text{Fe}_2\text{O}_5$. One of the critical aspects of the thermochemical CO_2 splitting is achieving maximum conversion as low conversion leads to use of excess CO_2 , thus increasing energy penalty associated with the process along with escalation in operating cost. When unmodified iron oxide is used as an oxygen carrier for thermochemical CO_2 splitting, it is typically reduced to Fe/FeO mixture [72]. This reduced iron oxide is then oxidized in CO_2 to produce CO. However, conversion of CO_2 to CO is thermodynamically limited. It must be noted that for unmodified iron oxide, iron can be oxidized in CO_2 only from Fe (0) to Fe (II, III) phase [12]. As a result, an additional air oxidation step must be used to obtain the fully oxidized Fe (III) phase to complete. However, the use of $\text{Ca}_2\text{Fe}_2\text{O}_5$ as an oxygen carrier overcomes this limitation. As seen from Eq. (2), iron can be oxidized completely from Fe (0) to Fe (III) in presence of CaO. Higher CO_2 conversion is obtained at any given temperature for $\text{Ca}_2\text{Fe}_2\text{O}_5$ as compared to unmodified iron oxide due to the synergistic effect between CaO and Fe, which lowers the oxidizing potential required for regeneration of Fe (0) using CO_2 . As seen in Fig. 3, CO_2 conversion close to 80% is obtained when the oxidizer is operated at 800°C and it drops to 75% as operating temperature is raised to 1100°C , pertaining to the exothermic nature of the reaction. High CO_2 conversion values enable significant reduction in parasitic energy requirement for CO_2 splitting.

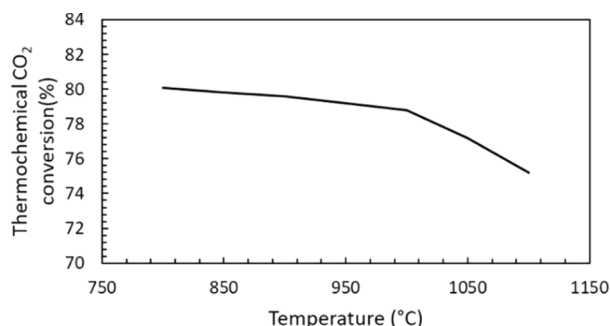


Fig. 3. Thermochemical CO_2 conversion vs. Temperature.

3.2. Solid conversion and morphological evolution

The freshly prepared oxygen carrier samples were characterized using EDS to get the distribution of various elements, as shown in Fig. S4. For unsupported $\text{Ca}_2\text{Fe}_2\text{O}_5$, elemental Ca and Fe were found to be distributed evenly across the surface with no agglomerates visible. Similarly, MgO was found to be well dispersed throughout the MgO-supported $\text{Ca}_2\text{Fe}_2\text{O}_5$ sample. Small dark areas in the EDS elemental mapping were present due to the shadowing created by uneven surface of the sample. Results from the EDS analysis confirmed that all the oxygen carriers prepared using solid state synthesis had homogeneous composition.

3.2.1. Thermogravimetric analysis

Although no interaction was found between the inert support MgO and the active metal oxide $\text{Ca}_2\text{Fe}_2\text{O}_5$ using EDS and XRD spectra, two samples-CF-0 Mg and CF-40 Mg were subjected to H_2 -TPR to investigate the change in oxygen carrier reducibility because of adding MgO to the oxygen carrier. As seen in Fig. 4, both the oxygen carriers started to show reactivity towards H_2 at $\sim 479^\circ\text{C}$ with CF-40 Mg showing higher reactivity as compared to CF-0 Mg. Similar results were obtained for the other two MgO-supported samples. Significant weight loss was observed at $\sim 800^\circ\text{C}$ for both the oxygen carriers suggesting the loss of lattice oxygen. No significant change was observed in the weight loss trend due to any catalytic promotion of the oxygen carrier by MgO addition, implying MgO addition enhanced the performance of the oxygen carriers by providing higher surface area and better dispersion of active metal oxide, without any kind of chemical interaction with the active species.

The effect of adding different concentrations of MgO to $\text{Ca}_2\text{Fe}_2\text{O}_5$ on CH_4 oxidation at 1000°C can be seen in Fig. 5a. Weight loss was observed roughly after 25 s of methane injection in all the samples, caused due to the time taken by weighing balance of the TGA to adjust itself to the change in buoyancy due to introduction of CH_4 along with N_2 for sample reduction. Rapid weight loss was observed for all the samples with the rate of loss and extent of reduction depending on the concentration of MgO added. The rate of weight loss for all the samples was high for first 20–25 s and slowed down gradually. For the first redox cycle, solid conversions (reduction) of 18.38%, 20.98%, 21.60% and 26.24% were obtained for 0, 10, 20 and 40% MgO loading, respectively.

Solid conversion and rate of reduction increased with the increase in MgO concentration in the sample. For analysing the weight change data from the TGA, the following equations were used:

$$\text{Solid conversion - reduction (\%)} : \frac{M_o - M_r}{[O]} \times 100 \quad (10)$$

$$\text{Solid conversion - oxidation (\%)} : \frac{M_{ro} - M_r}{[O]} \times 100 \quad (11)$$

M_o is the weight of fully oxidized sample, M_r is the weight of sample after

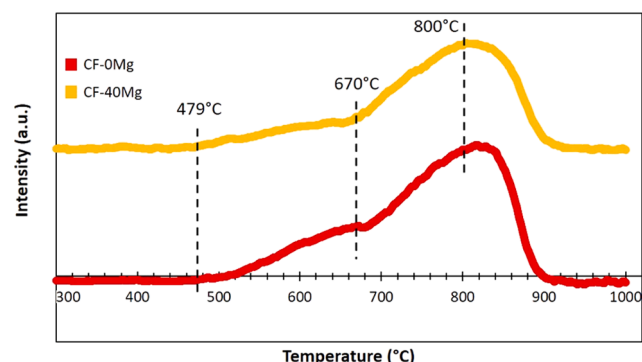


Fig. 4. TPR plot showing rate of weight change with temperature.

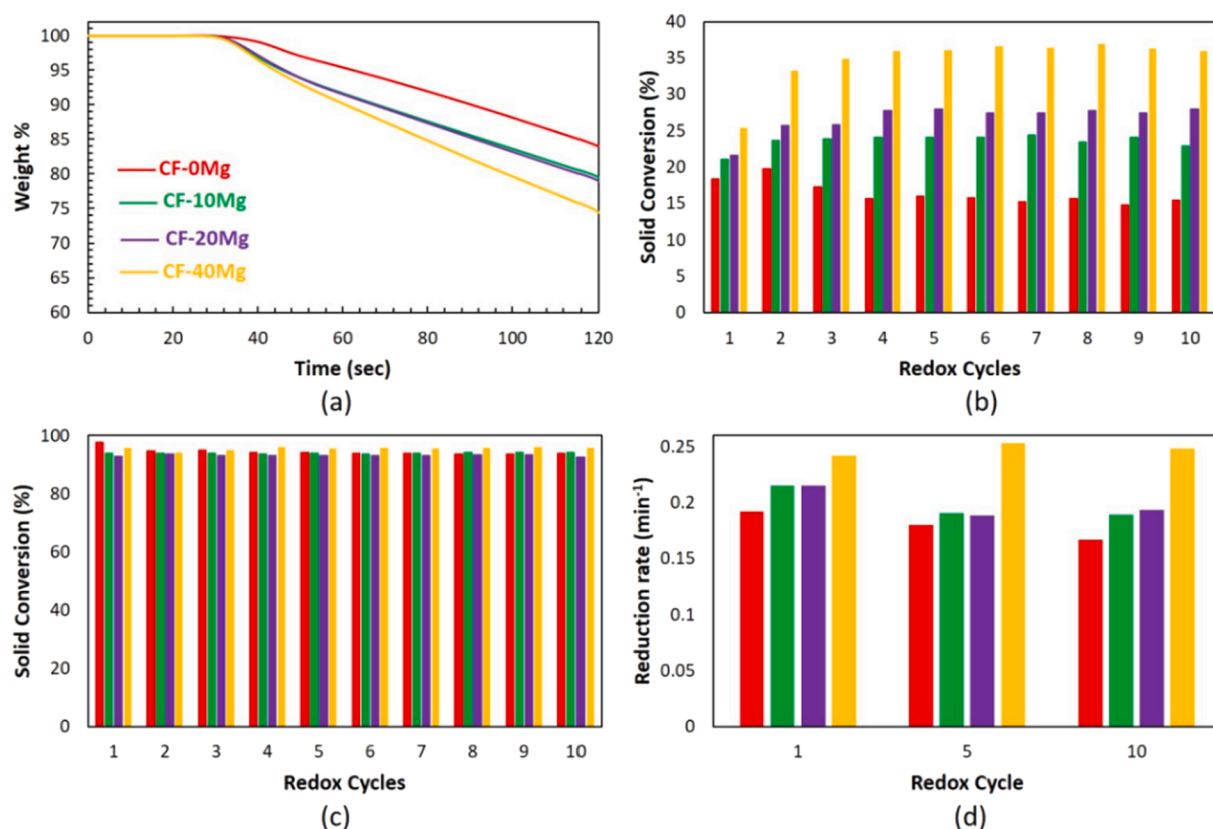


Fig. 5. (a) Weight change with time; (b) solid conversion-reduction and (c) solid conversion-CO₂ splitting over 10 isothermal redox cycles at 1000 °C, 1 atm and (d) Reduction rate at 1st, 5th, and 10th redox cycle.

2 min of reduction, M_{ro} is the weight of regenerated oxygen carrier, and $[O]$ is the theoretical amount of lattice oxygen present in the sample. The solid conversion during oxidation was normalized and then reported to have a better understanding of the results. As seen from Fig. 5b, the solid conversion (reduction) improved over redox cycles as the sample got activated in the process through phase stabilization [23]. Presence of MgO along with Ca₂Fe₂O₅ significantly increased the solid conversion during reaction, which is attributed to the high degree of dispersion of the active metal oxide over the entire surface, as confirmed through the EDS elemental mapping. For unsupported Ca₂Fe₂O₅, the solid conversion increased initially due to activation and then dropped over next few redox cycles before stabilizing. This drop in the solid conversion was due to sintering of sample, which causes a significant drop in the specific surface area due to formation of crystalline agglomerates, leading to a drop in the reactivity. Adding MgO as support prevented the sintering of Ca₂Fe₂O₅ and imparted stability to it. To ensure that this behavior was only due to sintering and not due to formation of a stable unreactive phase across redox cycles, similar experiment was performed using air as oxidant and the results are reported in supplementary section. The results from Fig. S5 show that the solid conversion dropped over cycles using air as the oxidant thus confirming sintering of the oxygen carrier sample.

To analyse the performance of different oxygen carrier samples during reduction across 10 redox cycles, the reduction rate was calculated and plotted as shown in Fig. 5d. The weight change data (solid conversion) during the reduction step was plotted as a function of time and a polynomial equation was obtained to describe the change in solid conversion with time. The equation was then differentiated with respect to time and the reduction rate was obtained. Reduction rate of CF-0 Mg decreased with multiple redox cycles, which occurred due to sintering of sample at high temperature. Oxygen carrier samples CF-10 Mg and CF-20 Mg showed higher reactivity for the first cycle, which dropped by

~12% till 5th redox cycle and remained almost same till 10th redox cycle was completed. CF-40 Mg showed the highest reduction rate amongst all the samples. The reduction rate of CF-40 Mg was higher than CF-0 Mg by ~20% and ~50% at 1st and 10th redox cycles, respectively. Even after 10 redox cycles, the reduction rate of CF-40 Mg did not change significantly and remained comparable to the rate observed at 1st redox cycle, suggesting 40% MgO support stabilized the active components (CaO and Fe₂O₃) of the oxygen carrier, thus enhancing its performance. CF-40 Mg was further subjected to 100 redox cycles in TGA using the experimental conditions as described in Section 2.2. As seen from Fig. 6, the oxygen carrier sample maintained its reactivity and recyclability across extended number of redox cycles, suggesting no loss of activity due to sintering or phase segregation.

3.2.2. Morphological evolution of the oxygen carrier

For MgO-supported Ca₂Fe₂O₅, solid conversion increased for first few cycles and then stabilized as steady-state conversion was reached

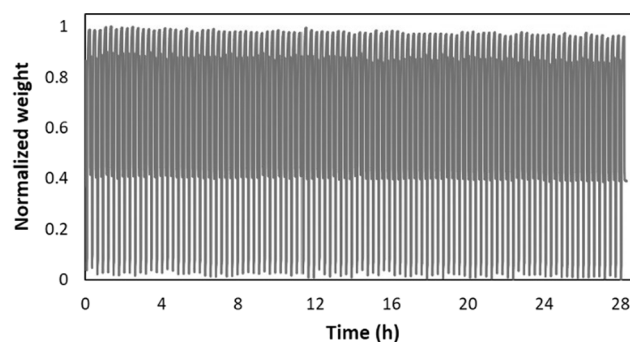


Fig. 6. CF-40 Mg subjected to isothermal redox cycles at 1000 °C, 1 atm.

without any drop in solid conversion, suggesting an improved tolerance of $\text{Ca}_2\text{Fe}_2\text{O}_5$ towards sintering. Fresh and post-redox oxygen carrier samples were subjected to SEM analysis to assess the effect of multiple redox cycles on the morphology of the oxygen carriers as shown in Fig. 7.

Increase in grain size by $\sim 11.7\%$ and agglomeration of sample was observed for unsupported $\text{Ca}_2\text{Fe}_2\text{O}_5$ caused due to sintering of sample at elevated operating temperature. MgO-supported sample was found to be more porous and agglomeration-free as compared to the unsupported one, as seen from the micrographs. The porous structure of the sample was maintained across multiple redox cycles, with no considerable difference between the grain sizes of the fresh and the post-redox sample as seen in Fig. 7c and d. Cyclic redox experiments were carried out in TGA to not only assess the reactivity of oxygen carrier samples towards CH_4 , but also understand the oxidation behavior of different samples. Fig. 5c shows the change in solid conversion during oxidation for different oxygen carrier samples over 10 redox cycles. All the oxygen carriers maintained steady solid conversion greater than 93%, implying stable performance of $\text{Ca}_2\text{Fe}_2\text{O}_5$ across multiple regeneration cycles. Complete conversion of reduced $\text{Ca}_2\text{Fe}_2\text{O}_5$ sample was not achieved due to increased gas diffusion resistance provided by product layers formed on the oxygen carrier. XRD results, as shown in Fig. 8 showed no presence of compounds such as $\text{Fe}_3\text{C}/\text{CaCO}_3$ that cannot be oxidized using CO_2 , along with no Fe_3O_4 formation indicating no Ca-Fe phase segregation across multiple redox cycles.

This was also confirmed by performing EDS mapping of the samples post redox, which showed the distribution of Ca-Fe-O similar to the fresh sample. The performance of unsupported $\text{Ca}_2\text{Fe}_2\text{O}_5$ was comparable to the samples with 10 and 20% MgO loading with solid conversion close to $\sim 93\%$. When MgO loading was increased to 40%, solid conversion $> 95\%$ was obtained. The improvement in solid conversion can be

attributed to presence of Mg^{2+} ions in $\text{Ca}_2\text{Fe}_2\text{O}_5$ crystal lattice, which help in creating vacancies and promote ionic diffusion through the solid [73]. Results from the cyclic experiments revealed that the direct conversion of $\text{Fe}(0)$ to $\text{Fe}(\text{III})$ was possible when $\text{Ca}_2\text{Fe}_2\text{O}_5$ is used as oxygen carrier, thus higher CO yield can be obtained as compared to unmodified iron oxide where $\text{Fe}(0)$ is oxidized to $\text{Fe}(\text{II,III})$ only due to thermodynamic constraints leading to incomplete regeneration of the oxygen carrier.

3.3. Simulated co-current moving bed experiments

Fig. 9 shows the outlet gas concentrations of various streams for the simulated co-current moving bed experiment using the CF-40 Mg oxygen carrier. Syngas selectivity of 98.08% was obtained for CF-40 Mg, which is $\sim 8.2\%$ higher than Fe_2O_3 as shown in Table 3. Similarly, an increase of $\sim 3.6\%$ (percentage points) in CH_4 conversion was obtained for CF-40 Mg as compared to Fe_2O_3 . Apart from the high selectivity towards generation of partial oxidation products at the top of the bed, the reduced solids present at the bottom convert any residual $\text{CO}_2/\text{H}_2\text{O}$ to CO/H_2 , thereby further enhancing the syngas yield. Synergy provided by using the highly reactive and syngas-selective $\text{MgO}-\text{Ca}_2\text{Fe}_2\text{O}_5$ oxygen carrier along with the co-current moving bed configuration enabled high fuel conversion with enhanced selectivity towards syngas production. Partially oxidized sample present at the bottom of the bed (oxidized by $\text{H}_2\text{O}/\text{CO}_2$) also provides lattice oxygen to methane that escapes the top portion of the moving bed, thus ensuring almost complete methane conversion. Methane conversion of $\sim 99.9\%$ was observed for the CF-40 Mg sample. Syngas with $\text{H}_2:\text{CO}$ ratio of ~ 2.0 was produced using CF-40 Mg sample as compared to 2.82 for Fe_2O_3 -based oxygen carrier. This high $\text{H}_2:\text{CO}$ ratio was obtained for the Fe_2O_3 case due to significant carbon deposition as reported by Kang et. al. [74]. The MgO supported

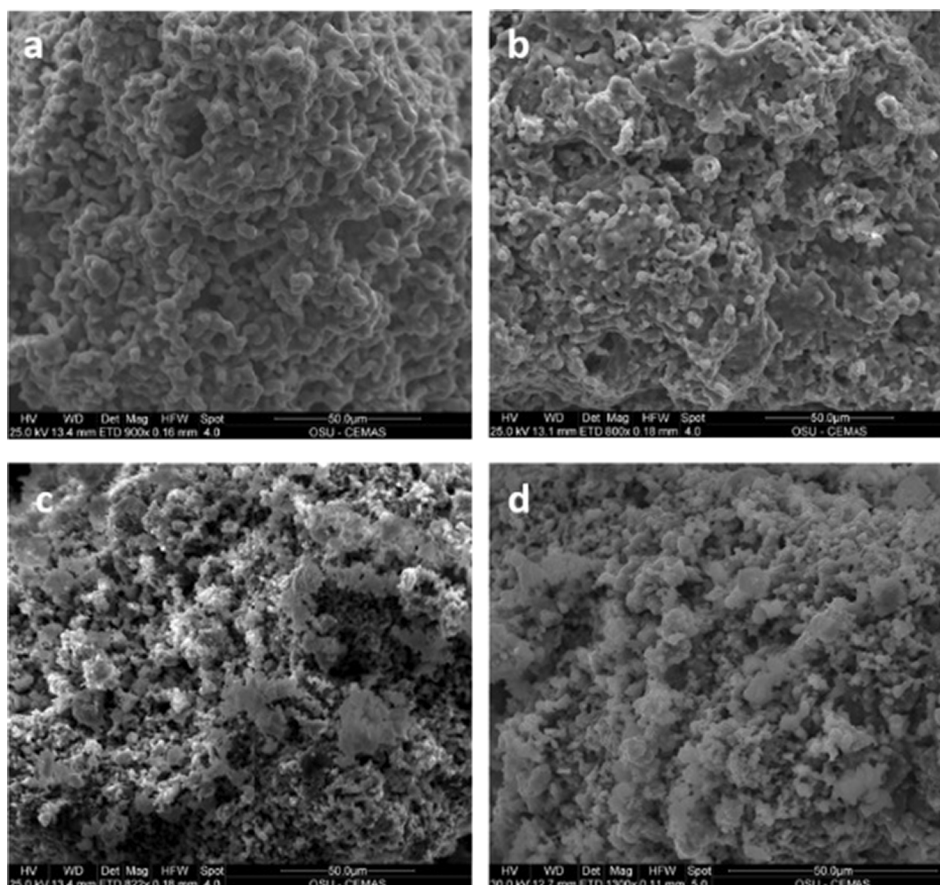


Fig. 7. SEM images showing Fresh (a) CF-0 Mg and (c) CF-40 Mg; and fully regenerated (b) CF-0 Mg and (d) CF-40 Mg after 10 redox cycles.

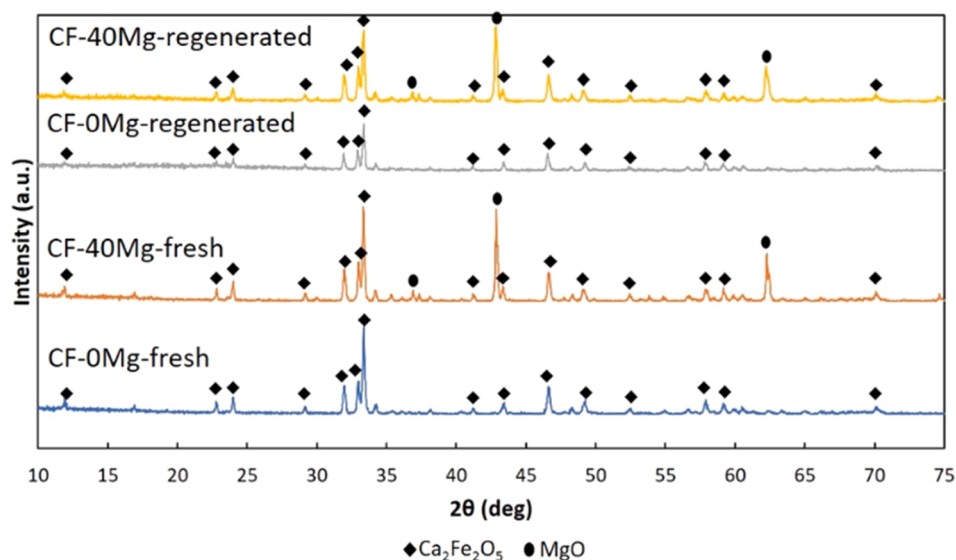


Fig. 8. XRD spectra of fresh and regenerated oxygen carrier samples after 10 redox cycles.

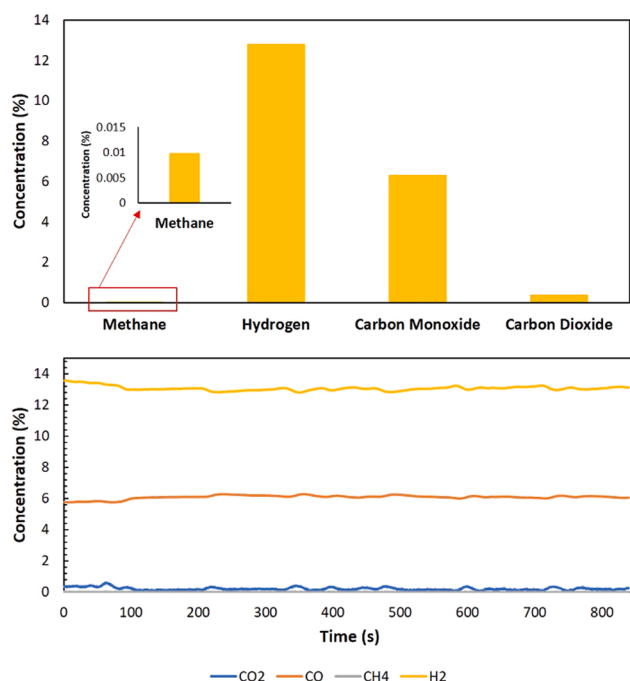


Fig. 9. Gas concentrations from simulated co-current moving bed setup for the CF-40 Mg oxygen carrier.

Table 3

Performance of the oxygen carriers in a simulated moving bed reactor.

Sample name	CH ₄ conversion (%)	Syngas selectivity (%)	H ₂ :CO ratio
CF-40 Mg	99.88	98.08	2.03
Fe ₂ O ₃ /Al ₂ O ₃	96.26	89.82	2.82

sample showed high tolerance to sintering and maintained its porous structure, behavior similar to that observed in the cyclic TGA tests. These results show MgO-supported Ca₂Fe₂O₅ exhibits higher activity for CH₄ partial oxidation as compared to the Fe₂O₃-based oxygen carrier [74–76]. Regeneration of the reduced oxygen carriers was performed using CO₂ as oxidant. CO₂ conversion of ~78% was obtained for both CF-0 Mg and CF-40 Mg, which was close to the thermodynamic

conversion as shown in Fig. 3. Gas concentration plots pertaining to CO₂ oxidation of the reduced oxygen carrier are presented in Fig. S6 of the supplementary section. CO₂ and CO concentrations (by vol.) of ~9% and ~30%, respectively were obtained during regeneration, corresponding to the CO yield of ~0.79 mols per mol of CO₂. The oxidized solids were further subjected to a check in the TGA, which confirmed complete oxidation of the oxygen carriers. These results ascertain that both reduction as well as the regeneration of the Ca₂Fe₂O₅-based oxygen carriers can be carried out close to the thermodynamic limits.

To assess long term performance of the oxygen carrier, CF-40 Mg was subjected to 5 continuous redox cycles in a simulated co-current moving bed setup. Different performance parameters related to the sample across 5 redox cycles can be seen in Fig. 10, where the steady state values of CH₄ conversion, syngas selectivity, and H₂:CO ratio have been reported. Consistent performance of the oxygen carrier was observed over 5 redox cycles, with no change in the time required to attain steady state. This finding suggested that MgO-supported Ca₂Fe₂O₅ is capable of generating high-quality syngas while getting completely regenerated in CO₂ without any reactivity loss because of high temperature sintering. Coupling these results with the long-term performance from the TGA depicted in Fig. 6 implied that Ca₂Fe₂O₅ is highly suitable for methane reforming as it has fast reaction kinetics as well as high thermodynamic selectivity towards syngas production.

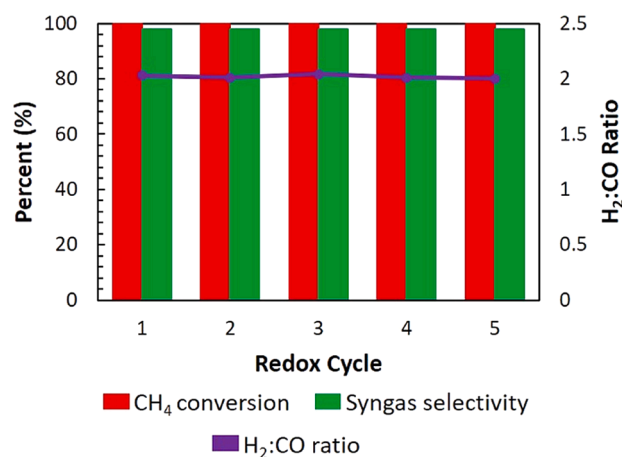


Fig. 10. Variation in process parameters with redox cycles conducted in a simulated co-current moving bed setup.

3.4. Theoretical study of the structure effect on reactivity

To gain a mechanistic insight into the mechanism for the reactivity enhancement, CH₄ adsorption and dissociation on Ca₂Fe₂O₅ (001) and Fe₂O₃(001) surface with oxygen vacancies was investigated using DFT + U calculations. The use of periodic models eliminates the edge effects and allows for a more accurate description of surface relaxation. Ca₂Fe₂O₅, also known as brownmillerite can be described as the structure with layers alternating between corner-sharing octahedra and tetrahedra. Depending on the cleavage position and the ordering of iron, calcium and oxygen atoms, two models were built: Fe-O terminated surface and Ca-O terminated surface as shown in Fig. 11. It was found that the surface free energy of the Fe-O terminated surface is 1.09 J/m², which is lower than the free energy of Ca-O terminated surface (1.92 J/m²). Therefore, the slab with Fe-O terminated surface was used to investigate the oxygen vacancy formation during CH₄ partial oxidation. On this slab, three chemically distinguishable types of lattice oxygen atoms are presents: lattice oxygen in corner-sharing octahedra O_(o), lattice oxygen in tetrahedra O_(t) and lattice oxygen between corner-sharing octahedra and tetrahedra O_(ot). The calculated formation energy for O_(o), O_(t) and O_(ot) are 205.81 kJ/mol, 259.85 kJ/mol and 311.72 kJ/mol respectively. It indicates the oxygen vacancy prefers to form at the octahedral sites as compared to the tetrahedral sites.

In CLRS process, CH₄ is initially dissociated over oxygen carriers to produce hydrogen and CH_x radicals. Then the CH_x radicals are oxidized by lattice oxygen to generate CO or CO₂. The relationship between C-H bond cleavage barrier and oxygen vacancy concentration of Ca₂Fe₂O₅ (001) surface was plotted in Fig. 12. The activation barrier of C-H bond in CH₄ decreases to 144.27 kJ/mol from 189.23 kJ/mol when the oxygen vacancy concentration increases to about 4.5%, then remains almost unchanged even though more oxygen vacancies are created. For the activation barrier of C-H bond in CH₃ radical, it decreases to 82.67 kJ/mol from 129.57 kJ/mol when the oxygen vacancy concentration increases to 4.5%, then remains at about 82 kJ/mol. The similar trend is observed in the activation of C-H bond in CH₂, the lowest barrier is obtained (63.06 kJ/mol) when the oxygen vacancy concentration reaches about 5%. For the activation of C-H bond in CH radical, the lowest barrier is 82.19 kJ/mol and the corresponding oxygen vacancy concentration is 4.4%. The relationship between C-H bond cleavage barrier and oxygen vacancy concentration of Fe₂O₃ (001) surface also was plotted in Fig. 12. It can be seen C-H cleavage barriers of CH₃, CH₂ and CH on Ca₂Fe₂O₅ (001) are about 10 kJ/mol lower than the barriers for

Fe₂O₃ (001) when the vacancy concentration is higher than 3%, indicating Ca₂Fe₂O₅ is more active for CH₄ dissociation than Fe₂O₃.

After the last C-H bond is cleaved, the lattice oxygen diffuses from the octahedral layers in the bulk to the surface vacancy site, to form a C-Fe-O species, which then converts to a gaseous CO molecule by Fe-C bond breaking. The Ca atoms, which are ordered into the oxygen layers between the layers of four coordinated Fe ions and the layers of octahedral Fe ions, migrate toward to the tetrahedral layer due to the oxygen vacancy formation. It leads to a high energy barrier of 93.82 kJ/mol for the diffusion of the lattice oxygen in the tetrahedral layer to the same vacancy to form CO₂. The energy profile of CO and CO₂ formation along with CH₄ dissociation on Ca₂Fe₂O₅ (001) and Fe₂O₃ (001) with oxygen vacancies were mapped in Fig. 13a. It shows the barrier of CO formation on reduced Ca₂Fe₂O₅ is 25.89 kJ/mol, which is 31.92 kJ/mol lower than the barrier obtained from the reduced Fe₂O₃ (001). The low barrier with respect to CO formation and CO desorption on Ca₂Fe₂O₅ (001) is attributed to the low formation energy of oxygen vacancy at the octahedral sites. It is worth noting that if two H atoms at two neighbouring O_(o) sites of the Ca₂Fe₂O₅ (001) surface directly approach each other to form H₂, it needs to overcome a high energy barrier of 229.32 kJ/mol due to the strong O-H bonds and the lack of active sites. This process is highly endothermic with a reaction energy of 68.55 kJ/mol. Thus, H₂ formation via binding two H atom from hydroxyl groups on the surface is both kinetically and thermochemically unfavourable. Alternatively, if one H atom migrates from the O_(o) site to the Fe site and then binds to another H atom at the O site, the H₂ formation barrier can be dramatically reduced to 102.56 kJ/mol. These results indicate that the lattice oxygen in corner-sharing octahedra O_(o) acts as efficient active sites for CO and H₂ production. The overall reaction mechanism based upon the thermodynamic analysis, redox experiments and DFT calculations is shown in Fig. 13b. Near 100% selectivity towards syngas is obtained due to favourable thermodynamics as well as the unique brownmillerite structure of the oxygen carrier coupled with the use of co-current moving bed type design of the reactor. Although MgO is used as the support of calcium ferrite oxygen carrier, it does not actively take part in redox reactions but enhances the sintering resistance of the material to increase its recyclability as shown in Fig. 5.

4. Conclusion

Different Ca-Fe based oxygen carrier samples were synthesized to study methane reforming coupled with thermochemical splitting of CO₂

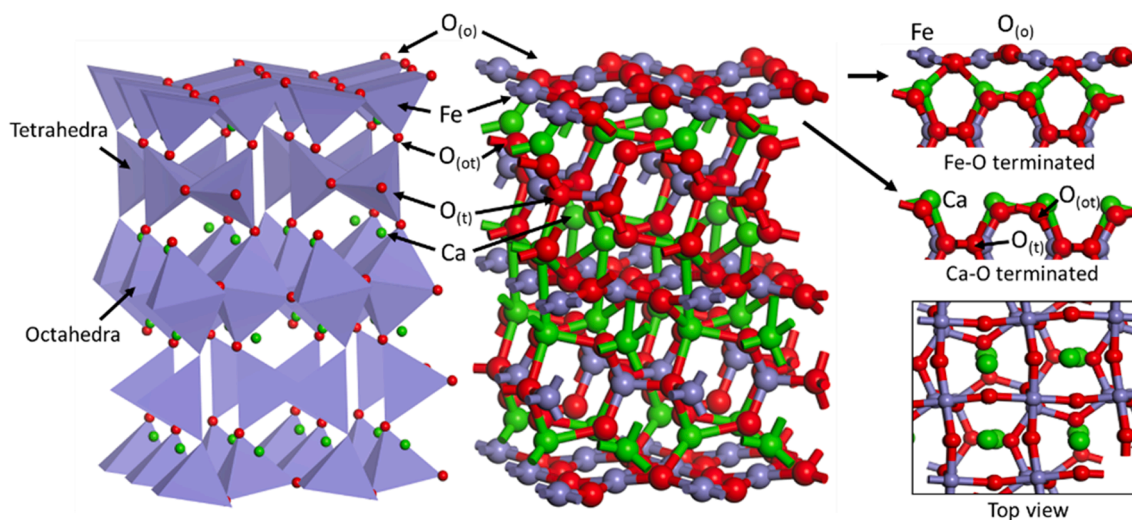


Fig. 11. Ca₂Fe₂O₅ (001) surface with layers alternating between corner-sharing octahedra and tetrahedra. Iron atoms are displayed as purple balls, Calcium atoms as green balls and lattice oxygen atoms as red balls. Side view of different surface terminations and top view of the surface are given. (For interpretation of the references to color in this figure legend, the reader is referred to the web version of this article.)

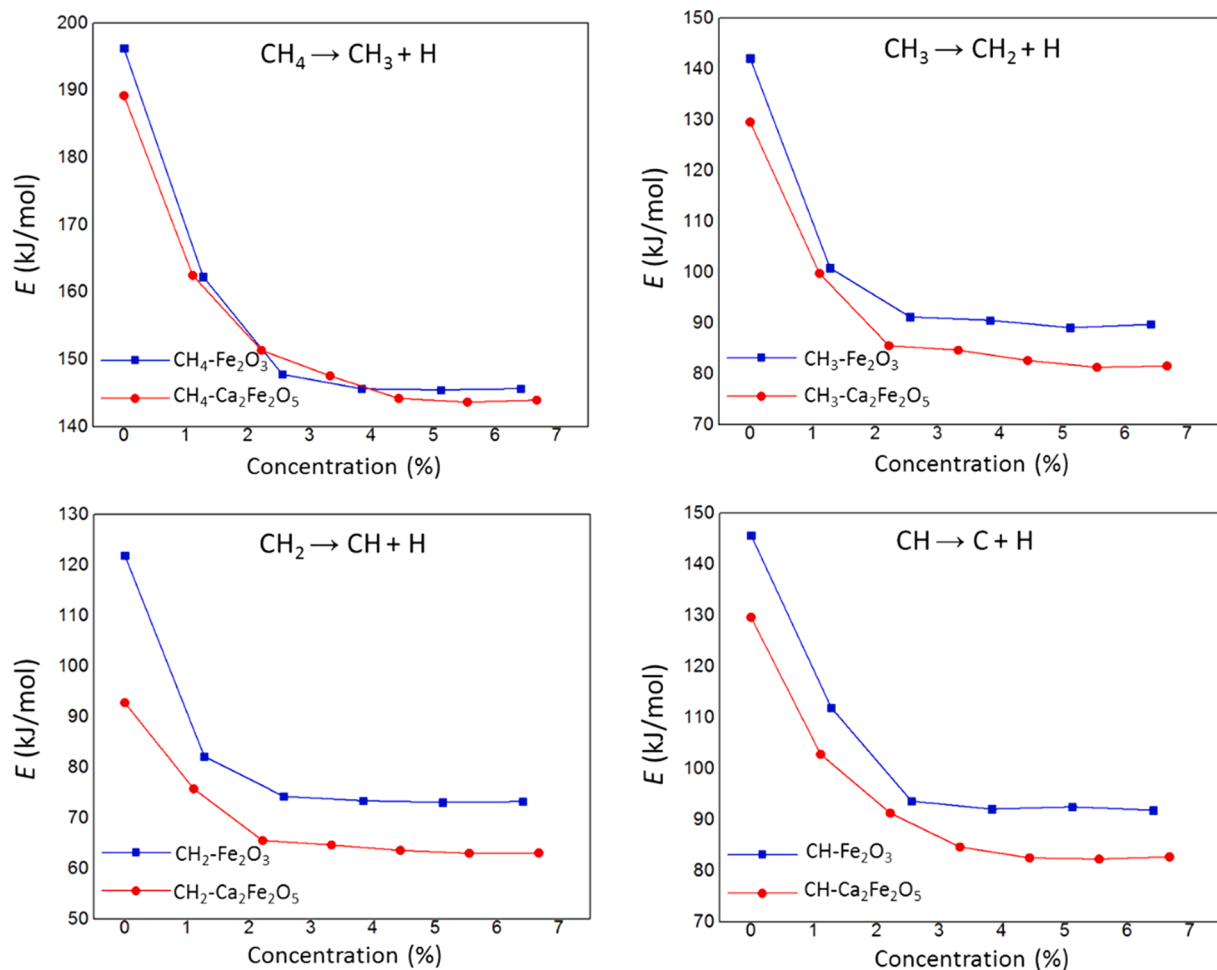


Fig. 12. The effect of oxygen vacancy concentration on the energy barrier of C-H bond cleavage on $\text{Ca}_2\text{Fe}_2\text{O}_5$ (001) and Fe_2O_3 (001).

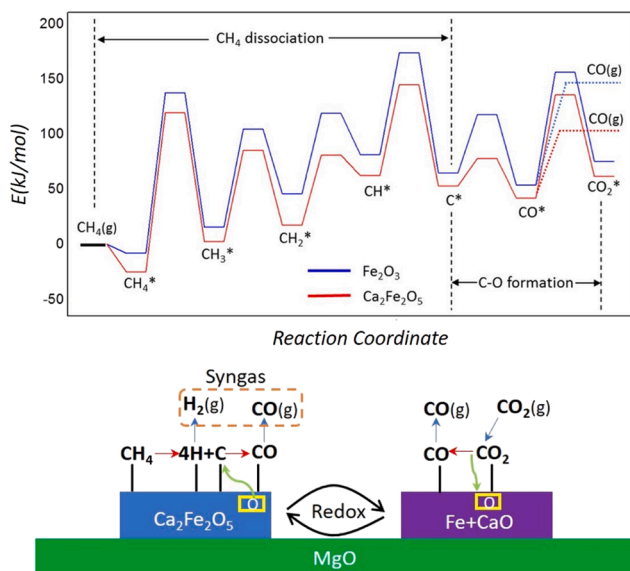


Fig. 13. (a) The calculated energy profiles for CH_4 dissociation and CO/CO_2 formation on $\text{Ca}_2\text{Fe}_2\text{O}_5$ (001) and Fe_2O_3 (001), (b) proposed overall reaction mechanism. (g) Denotes in gas phase.

using the novel CLRS process. Thermodynamic analysis indicated that $\text{Ca}_2\text{Fe}_2\text{O}_5$ oxygen carriers give superior performance for syngas production as compared to Fe_2O_3 . Also, the use of $\text{Ca}_2\text{Fe}_2\text{O}_5$ leads to a higher thermodynamic CO_2 conversion upon oxidation of the reduced samples. MgO-supported $\text{Ca}_2\text{Fe}_2\text{O}_5$ oxygen carriers were prepared to examine the support effect on the performance of the oxygen carriers in the CLRS process. CH_4 conversion >99% with syngas selectivity ~98% and H_2/CO ratio 2:1 was obtained for 40% MgO-supported sample by using simulated co-current moving bed experiments. Complete regeneration was achieved with CO_2 conversion of ~78%. It was found that addition of MgO imparted a porous structure to the oxygen carriers, thus improving the stability and the recyclability of $\text{Ca}_2\text{Fe}_2\text{O}_5$. MgO-supported $\text{Ca}_2\text{Fe}_2\text{O}_5$ was able to maintain its reactivity and recyclability over 100 continuous redox cycles in a TGA, while also generating high-quality syngas consistently across 5 redox cycles as observed in the simulated co-current moving bed setup. Density functional theory calculations reveal that the brownmillerite structure possessed by $\text{Ca}_2\text{Fe}_2\text{O}_5$ facilitates oxygen vacancy formation that promotes the methane activation and dissociation. Further, exceptionally high syngas selectivity has also been explained to be due to the low energy barrier of CO formation through lattice oxygen migration in the layers alternating between corner-sharing octahedra and tetrahedra. This study proves that MgO supported $\text{Ca}_2\text{Fe}_2\text{O}_5$ can serve as an efficient oxygen carrier for simultaneously producing high purity syngas as well as splitting CO_2 to CO via a novel moving-bed chemical looping process and will impact future chemical looping system design.

CRediT authorship contribution statement

Vedant Shah: Conceptualization, Investigation, Data curation, Validation, Formal analysis, Resources, Writing - original draft. **Zhuo Cheng:** Investigation, Software, Formal analysis, Data curation, Formal analysis, Validation, Writing - review & editing. **Deven S. Baser:** Writing - review & editing. **Jonathan A. Fan:** Supervision, Writing - review & editing. **Liang-Shih Fan:** Supervision, Writing - review & editing.

Declaration of Competing Interest

The authors declare that they have no known competing financial interests or personal relationships that could have appeared to influence the work reported in this paper.

Acknowledgement

The authors would like to acknowledge the service provided by Center for Electron Microscopy and Analysis (CEMAS) and Ohio Supercomputer Center (OSC). Helpful discussion with Kalyani Jangam is also acknowledged by the authors.

Funding Source

This research did not receive any specific grant from funding agencies in the public, commercial, or not-for-profit sectors.

Appendix A. Supplementary material

Supplementary data to this article can be found online at <https://doi.org/10.1016/j.apenergy.2020.116111>.

References

- [1] Yokota O, Tanaka T, Hou Z, Yashima T. Hexaaluminate catalysts of the novel process of syngas production through catalytic oxidation and steam- CO_2 reforming of methane. *Stud Surf Sci Catal* 2004;153:141–4.
- [2] Bezdek RH. The hydrogen economy and jobs of the future. *Renew Energy Environ Sustain* 2019;4:1.
- [3] Simbeck DR, Karp AD, Dickenson RL. Syngas production for gas-to-liquids applications: technologies, issues and outlook. *Fuel Process Technol* 2001;1–3: 139–48.
- [4] Figen HE, Baykara SZ. Effect of ruthenium addition on molybdenum catalysts for syngas production via catalytic partial oxidation of methane in a monolithic reactor. *Int J Hydrogen Energy* 2018;43:1129–38.
- [5] Aasberg-Petersen K, Christensen TS, Stub Nielsen C, Dybkjær I. Recent developments in autothermal reforming and pre-reforming for synthesis gas production in GTL applications. *Fuel Process Technol* 2003;83:253–61.
- [6] Neiva L. A study on the characteristics of the reforming of methane: a review. *Brazilian J Pet Gas* 2010;4(3):119–27.
- [7] Arvanitis A, Sun X, Yang S, Damma D, Smirniotis P, Dong J. Approaching complete CO conversion and total H_2 recovery for water gas shift reaction in a high-temperature and high-pressure zeolite membrane reactor. *J Memb Sci* 2018;549: 575–80.
- [8] Blumberg T, Morosuk T, Tsatsaronis G. A comparative exergoeconomic evaluation of the synthesis routes for methanol production from natural gas. *Appl Sci* 2017;7 (12):1213.
- [9] Ebrahimi H, Rahmani M. A new design for CO_2 capture and usage in a syngas production unit by carbonate chemical looping. *J Nat Gas Sci Eng* 2016;36:241–51.
- [10] Pullar RC, Novais RM, Caetano APF, Barreiros MA, Abanades S, Oliveira FAC. A review of solar thermochemical CO_2 splitting using ceria-based ceramics with designed morphologies and microstructures. *Front Chem* 2019;7:601.
- [11] Tou M, Michalsky R, Steinfeld A. Solar-driven thermochemical splitting of CO_2 and in situ separation of CO and O_2 across a ceria redox membrane reactor. *Joule* 2017; 1:146–54.
- [12] Fan L-S. Chemical looping systems for fossil energy conversions. Hoboken, NJ, USA: John Wiley & Sons, Inc.; 2010.
- [13] Zeng L, Cheng Z, Fan JA, Fan LS, Gong J. Metal oxide redox chemistry for chemical looping processes. *Nat Rev Chem* 2018;2(11):349–64.
- [14] Xu D, Zhang Y, Hsieh TL, Guo M, Qin L, Chung C, et al. A novel chemical looping partial oxidation process for thermochemical conversion of biomass to syngas. *Appl Energy* 2018;222:119–31.
- [15] Hsieh TL, Zhang Y, Xu D, Wang C, Pickarts M, Chung C, et al. Chemical looping gasification for producing high purity, H_2 -rich syngas in a cocurrent moving bed reducer with coal and methane cofeeds. *Ind Eng Chem Res* 2018;57(7):2461–75.
- [16] Zhu L, Tu J, Shi Y. Separation of $\text{CO-CO}_2\text{-N}_2$ gas mixture for high-purity CO by pressure swing adsorption. *Gas Sep Purif* 1991;5(3):173–6.
- [17] Zhu X, Wei Y, Wang H, Li K. Ce-Fe oxygen carriers for chemical-looping steam methane reforming. *Int J Hydrogen Energy* 2013;38(11):4492–501.
- [18] Luo S, Zeng L, Fan L-S. Chemical looping technology: oxygen carrier characteristics. *Annu Rev Chem Biomol Eng* 2015;6:53–75.
- [19] Li S, Krishnamoorthy S, Li A, Meitzner GD, Iglesia E. Promoted iron-based catalysts for the Fischer-Tropsch synthesis: design, synthesis, site densities, and catalytic properties. *J Catal* 2002;206(2):202–17.
- [20] Chen S, Shi Q, Xue Z, Sun X, Xiang W. Experimental investigation of chemical-looping hydrogen generation using Al_2O_3 or TiO_2 -supported iron oxides in a batch fluidized bed. *Int J Hydrogen Energy* 2011;36(15):8915–26.
- [21] Qin L, Cheng Z, Fan JA, Kopechek D, Xu D, Deshpande N, et al. Nanostructure formation mechanism and ion diffusion in iron–titanium composite materials with chemical looping redox reactions. *J Mater Chem A* 2015;3(21):11302–12.
- [22] Qin L, Guo M, Cheng Z, Xu M, Liu Y, Xu D, et al. Improved cyclic redox reactivity of lanthanum modified iron-based oxygen carriers in carbon monoxide chemical looping combustion. *J Mater Chem A* 2017;5(38):20153–60.
- [23] Chung C, Qin L, Shah V, Fan L-S. Chemically and physically robust, commercially-viable iron-based composite oxygen carriers sustainable over 3000 redox cycles at high temperatures for chemical looping applications. *Energy Environ Sci* 2017;10 (11):2318–23.
- [24] Chen YY, Nadgouda S, Shah V, Fan LS, Tong A. Oxidation kinetic modelling of Fe-based oxygen carriers for chemical looping applications: impact of the topochemical effect. *Appl Energy* 2020;279:115701.
- [25] Bhavsar S, Vesper G. Chemical looping beyond combustion: production of synthesis gas via chemical looping partial oxidation of methane. *RSC Adv* 2014;4:47254–67.
- [26] Zhang Y, Doroodchi E, Moghtaderi B. Chemical looping combustion of ultra low concentration of methane with $\text{Fe}_2\text{O}_3/\text{Al}_2\text{O}_3$ and CuO/SiO_2 . *Appl Energy* 2014; 113:1916–23.
- [27] Li K, Wang H, Wei Y. Syngas generation from methane using a chemical-looping concept: a review of oxygen carriers. *J Chem* 2013;2013:1–8.
- [28] Hafizi A, Rahimpour MR, Hassanajili S. Hydrogen production by chemical looping steam reforming of methane over Mg promoted iron oxygen carrier: optimization using design of experiments. *J Taiwan Inst Chem Eng* 2016;62:140–9.
- [29] Eichel R-A. Structural and dynamic properties of oxygen vacancies in perovskite oxides—analysis of defect chemistry by modern multi-frequency and pulsed EPR techniques. *Phys Chem Chem Phys* 2011;13:368–84.
- [30] Nalbandian L, Eydou A, Zaspalis V. $\text{La}_{1-x}\text{Sr}_x\text{M}_y\text{Fe}_{1-y}\text{O}_{3-8}$ perovskites as oxygen-carrier materials for chemical-looping reforming. *Int J Hydrogen Energy* 2011;36: 6657–70.
- [31] Tang M, Xu L, Fan M. Progress in oxygen carrier development of methane-based chemical-looping reforming: a review. *Appl Energy* 2015;151:143–56.
- [32] Nadgouda SG, Guo M, Tong A, Fan LS. High purity syngas and hydrogen coproduction using copper-iron oxygen carriers in chemical looping reforming process. *Appl Energy* 2019;235:1415–26.
- [33] Baser DS, Nadgouda SG, Joshi AS, Fan LS. 110th anniversary: indirect partial oxidation of methane using a counter-current moving-bed chemical looping configuration for enhanced syngas production. *Ind Eng Chem Res* 2019;58(36): 16407–16.
- [34] Chan MSC, Liu W, Ismail M, Yang Y, Scott SA, Dennis JS. Improving hydrogen yields, and hydrogen: steam ratio in the chemical looping production of hydrogen using $\text{Ca}_2\text{Fe}_2\text{O}_5$. *Chem Eng J* 2016;296:406–11.
- [35] Ismail M, Liu W, Dunstan MT, Scott SA. Development and performance of iron based oxygen carriers containing calcium ferrites for chemical looping combustion and production of hydrogen. *Int J Hydrogen Energy* 2016;41:4073–84.
- [36] Shah V, Mohapatra P, Fan LS. Thermodynamic and process analyses of syngas production using chemical looping reforming assisted by flexible dicalcium ferrite-based oxygen carrier regeneration. *Energy Fuels* 2020;34(5):6490–500.
- [37] Shah V, Joshi R, Fan LS. Thermodynamic investigation of process enhancement in chemical looping reforming of methane through modified Ca-Fe oxygen carrier utilization. *Ind Eng Chem Res* 2020;59(35):15531–41.
- [38] Liu G, Liao Y, Wu Y, Ma X. Application of calcium ferrites as oxygen carriers for microalgae chemical looping gasification. *Energy Convers Manag* 2018;160: 262–72.
- [39] Liu G, Liao Y, Wu Y, Ma X. Reactivity of Co-doped $\text{Ca}_2\text{Fe}_2\text{O}_5$ brownmillerite oxides as oxygen carriers for microalgae chemical looping gasification. *Int J Hydrogen Energy* 2019;160:262–72.
- [40] Hosseini D, Donat F, Abdala PM, Kim SM, Kierzkowska AM, Müller CR. Reversible exsolution of dopant improves the performance of $\text{Ca}_2\text{Fe}_2\text{O}_5$ for chemical looping hydrogen production. *ACS Appl Mater Interfaces* 2019;11(20):18276–84.
- [41] Sun Z, Chen S, Hu J, Chen A, Rony AH, Russell CK, et al. $\text{Ca}_2\text{Fe}_2\text{O}_5$: A promising oxygen carrier for CO/CH_4 conversion and almost-pure H_2 production with inherent CO_2 capture over a two-step chemical looping hydrogen generation process. *Appl Energy* 2018;211:431–42.
- [42] Sun Z, Chen S, Russell CK, Hu J, Rony AH, Tan G, et al. Improvement of H_2 -rich gas production with tar abatement from pine wood conversion over bi-functional $\text{Ca}_2\text{Fe}_2\text{O}_5$ catalyst: Investigation of inner-looping redox reaction and promoting mechanisms. *Appl Energy* 2018;212:931–43.
- [43] Sun Z, Wu X, Russell CK, Dyar MD, Sklute EC, Toan S, et al. Synergistic enhancement of chemical looping-based CO_2 splitting with biomass cascade utilization using cyclic stabilized $\text{Ca}_2\text{Fe}_2\text{O}_5$ aerogel. *J Mater Chem A* 2019;7(3): 1216–26.

- [44] Löfberg A, Guerrero-Caballero J, Kane T, Rubbens A, Jalowiecki-Duhamel L. Ni/CeO₂ based catalysts as oxygen vectors for the chemical looping dry reforming of methane for syngas production. *Appl Catal B* 2017;212:159–74.
- [45] Zeng J, Xiao R, Zhang H, Wang Y, Zeng D, Ma Z. Chemical looping pyrolysis-gasification of biomass for high H₂/CO syngas production. *Fuel Process Technol* 2017;168:116–22.
- [46] Kang D, Lim HS, Lee M, Lee JW. Syngas production on a Ni-enhanced Fe₂O₃/Al₂O₃ oxygen carrier via chemical looping partial oxidation with dry reforming of methane. *Appl Energy* 2018;211:174–86.
- [47] Ding H, Xu Y, Luo C, Wang Q, Shen C, Xu J, et al. A novel composite perovskite-based material for chemical-looping steam methane reforming to hydrogen and syngas. *Energy Convers Manag* 2018;171:12–9.
- [48] Alirezaei I, Hafizi A, Rahimpour MR. Syngas production in chemical looping reforming process over ZrO₂ promoted Mn-based catalyst. *J CO₂ Util* 2018;23:105–16.
- [49] Osman M, Zaabout A, Cloete S, Amini S. Internally circulating fluidized-bed reactor for syngas production using chemical looping reforming. *Chem Eng J* 2019;377:120076.
- [50] Hu J, Li C, Zhang Q, Guo Q, Zhao S, Wang W, et al. Using chemical looping gasification with Fe₂O₃/Al₂O₃ oxygen carrier to produce syngas (H₂+ CO) from rice straw. *Int J Hydrog Energy* 2019;44(6):3382–6.
- [51] Liu C, Li S, Xiao Y, Li T, Wang W. Hydrogen-rich syngas production by chemical looping steam reforming of acetic acid as bio-oil model compound over Fe-doped LaNiO₃ oxygen carriers. *Int J Hydrog Energy* 2019;44(33):17732–41.
- [52] Yang J, Wei Y, Yang J, Xiang H, Ma L, Zhang W, et al. Syngas production by chemical looping gasification using Fe supported on phosphogypsum compound oxygen carrier. *Energy* 2019;168:126–35.
- [53] Liu G, Liao Y, Wu Y, Ma X. Enhancement of Ca₂Fe₂O₅ oxygen carrier through Mg/Al/Zn oxide support for biomass chemical looping gasification. *Energy Convers Manag* 2019;2019(195):262–73.
- [54] Hu Q, Shen Y, Chew JW, Ge T, Wang CH. Chemical looping gasification of biomass with Fe₂O₃/CaO as the oxygen carrier for hydrogen-enriched syngas production. *Chem Eng J* 2020;2020(379):122346.
- [55] Wang C, Yan H, Yu Y, Liang W, Yuan S, Cui W, et al. Chemical-looping reforming of coal tar vapor on the surface of CaO-modified Fe-based oxygen carrier. *Energy Fuels* 2020.
- [56] Durán-Martín JD, Jimenez PES, Valverde JM, Perejón A, Arcenegui-Troya J, Triñanes PG, et al. Role of particle size on the multicycle calcium looping activity of limestone for thermochemical energy storage. *J Adv Res* 2020;22:67–76.
- [57] Salaudeen SA, Acharya B, Dutta A. CaO-based CO₂ sorbents: A review on screening, enhancement, cyclic stability, regeneration and kinetics modelling. *J CO₂ Util* 2018;23:179–99.
- [58] Kathe MV, Empfield A, Na J, Blair E, Fan L-S. Hydrogen production from natural gas using an iron-based chemical looping technology: thermodynamic simulations and process system analysis. *Appl Energy* 2016;165:183–201.
- [59] Berman RG, Brown TH. Heat capacity of minerals in the system Na₂O-K₂O-CaO-MgO-FeO-Fe₂O₃-Al₂O₃-SiO₂-TiO₂-H₂O-CO₂: representation, estimation, and high temperature extrapolation. *Contrib Mineral Petrol* 1986;94(2):262.
- [60] Kresse G, Hafner J. Ab initio molecular dynamics for liquid metals. *Phys Rev B* 1993;47(1):558.
- [61] Kresse G, Furthmüller J. Efficiency of ab-initio total energy calculations for metals and semiconductors using a plane-wave basis set. *Comput Mater Sci* 1996;6(1):15–50.
- [62] Kresse G, Furthmüller J. Efficient iterative schemes for ab initio total-energy calculations using a plane-wave basis set. *Phys Rev B* 1996;54(16):11169–86.
- [63] Perdew JP, Burke K, Ernzerhof M. Generalized gradient approximation made simple. *Phys Rev Lett* 1997;77(18):3865–8.
- [64] Blöchl PE. Projector augmented-wave method. *Phys Rev B* 1994;50(24):17953–79.
- [65] Kresse G, Joubert D. From ultrasoft pseudopotentials to the projector augmented-wave method. *Phys Rev B* 1999;59(3):1758–75.
- [66] Blöchl PE, Jepsen O, Andersen OK. Improved tetrahedron method for Brillouin-zone integrations. *Phys Rev B* 1994;49:16223–33.
- [67] Herbst JF, Watson RE, Wilkins JW. Relativistic calculations of 4f excitation energies in the rare-earth metals: Further results. *Phys Rev B* 1978;17(8):3089–98.
- [68] Anisimov VI, Gunnarsson O. Density-functional calculation of effective Coulomb interactions in metals. *Phys Rev B* 1991;43(10):7570–4.
- [69] Sheppard D, Henkelman G. Paths to which the nudged elastic band converges. *J Comput Chem* 2011;32(8):1769–71.
- [70] Henkelman G, Uberuaga BP, Jónsson H. A climbing image nudged elastic band method for finding saddle points and minimum energy paths. *J Chem Phys* 2000;113(22):9901–4.
- [71] Bale CW, Bélisle E, Chartrand P, Decterov SA, Eriksson G, Gheribi AE, et al. Reprint of: FactSage thermochemical software and databases, 2010–2016. *Calphad* 2016;55:1–19.
- [72] Ambrosini A, Coker EN, Rodriguez MA, Livers S, Evans LR, Miller JE, et al. Synthesis and characterization of ferrite materials for thermochemical CO₂ splitting using concentrated solar energy. *ACS Symp Ser* 2010;1–13.
- [73] Słowiński G, Smoliński A. Thermodynamic feasibility of hydrogen-rich gas production supported by iron based chemical looping process. *J Chem* 2016;2016:1–5.
- [74] Kang D, Lee M, Lim HS, J W. Chemical looping partial oxidation of methane with CO₂ utilization on the ceria-enhanced mesoporous Fe₂O₃ oxygen carrier. *Fuel* 2018;215:787–98.
- [75] Luo S, Zeng L, Xu D, Kathe M, Chung E, Deshpande N, et al. Shale gas-to-syngas chemical looping process for stable shale gas conversion to high purity syngas with a H₂/CO ratio of 2:1. *Energy Environ Sci* 2014;7(12):4104–17.
- [76] Park C, Hsieh TL, Pottimurthy Y, Shah V, Xu D, Chen YY, et al. Design and operations of a 15 kWth subpilot unit for the methane-to-syngas chemical looping process with CO₂ utilization. *Ind Eng Chem Res* 2019;59(15):6886–99.